Evolution of droplets of perfectly wetting liquid under the influence of thermocapillary forces

Shomeek Mukhopadhyay,[1,4] Nebojsa Murisic,[2] Robert P. Behringer,[1] and Lou Kondic[3]
[1]*Department of Physics and Center for Complex Systems, Duke University, Durham, North Carolina 27706, USA*
[2]*Department of Mathematics, University of California, Los Angeles, Los Angeles, California 90095, USA*
[3]*Department of Mathematical Sciences, Center for Applied Mathematics and Statistics, New Jersey Institute of Technology, Newark, New Jersey 07102, USA*
[4]*Department of Chemistry, Columbia University, New York, New York 10027, USA*
(Received 14 August 2010; revised manuscript received 30 December 2010; published 5 April 2011)

We consider the evolution of sessile droplets of a nonvolatile perfectly wetting liquid on differentially radially heated solid substrates. The heating induces thermocapillary Marangoni forces that affect the contact line dynamics. Our experiments involving a particular heating pattern reveal that the Marangoni effect suppresses the spreading of a drop, typical for perfectly wetting liquids. The result is a rather slow receding motion and a distinctive thinning of the liquid layer in the region close to the contact line. Our theoretical model, based on the lubrication approximation and incorporating the Marangoni effect, recovers the main features observed in the experiments, and in addition predicts novel features that are still to be observed.

DOI: 10.1103/PhysRevE.83.046302 PACS number(s): 47.20.−k, 68.15.+e, 47.55.dm

I. INTRODUCTION

Thermally driven flows of thin liquid layers have attracted an ever increasing amount of attention in recent years, due to their applications in micro- and nanodevices [1,2]. Free-surface flows are particularly interesting as they allow for rapidly configurable devices, which, with minimal or no substrate modification, can lead to a significant increase in the device throughput [3]. Various applications clearly indicate the need for a more detailed understanding of the dynamics of these thermally driven flows, particularly in the vicinity of the (triple) contact line and in connection to its mobility [4–6].

Numerous theoretical studies of drops subject to thermal gradients have appeared in the literature. The wetting behavior of drops on a vertical surface subject to a temperature gradient was studied theoretically by Ehrhard and Davis [7], who found that the application of the temperature gradient either enhanced or suppressed the drop motion, depending on its direction. In their model, such behavior was attributed to thermocapillary flows within the drop, induced by solid heating. The modeling approach from [7] was subsequently used in synergy with the lubrication approximation in [8], where manipulation of drops using differential heating in the solid was studied, and in [9–11], where the stability of climbing films was examined. A similar approach was also used in [12], where the focus was on the role of the slip coefficient. The influence of a linear temperature profile on the drop motion and the connection to the phenomena of superspreading was studied theoretically in [13]. In [14,15], a theoretical model was derived to study the stability of thin liquid layers subject to out-of-plane temperature gradients where a nonlinear thermocapillary effect may be relevant. In [16], the breakup of thin liquid films into arrays of drops and their subsequent motion on slightly inclined uniformly heated solid substrates were studied theoretically; Newton's law of cooling was employed to take into account heat transfer from the film surface to the surrounding gas. A theoretical model was developed in [17] to study the influence of drop size on the motion of nanodroplets on chemically structured substrates. Reviews of various models used in studying thin films and drops in general were given in [6,18,19]. In particular, the importance of examining contact line motion for perfectly wetting liquids, including situations when the driving is by thermocapillary effects, was emphasized in [6].

Experimental studies have focused on fingering instabilities in thin films climbing a solid wall or an incline subject to differential heating [1,20], liquid drops migrating in vertical temperature gradients [21], stability of undercompressive shocks for draining thin films driven by a surface tension gradient against gravity [22], merging and condensation of drops subject to radial temperature gradients [23], and superspreading of drops on hydrophobic solid surfaces due to the Marangoni effect induced by the presence of surfactants [24]. In [25–27], experimental studies of falling films exposed to localized heating and bounded by vertical solid walls were carried out; an accompanying theoretical model was formulated in [27,28] and it explained the experimental results based on a competition between gravity and thermocapillary Marangoni stresses. In recent years, experiments have centered on using both chemical modification of the substrate surface and nonuniform heating for thermophoretic manipulation of droplets of partially wetting liquids [29].

Our present study focuses on the evolution of drops of perfectly wetting nonvolatile liquid under the influence of the thermocapillary Marangoni effect induced by differential heating of the solid substrate. We concentrate on a particular setup where perfectly wetting drops are subject to a radial temperature gradient. We will see that direct comparison of experiments and theory, as implemented in this paper, provides an effective approach for understanding the main features of the results, including perhaps unexpected drop shapes. The first part of the paper presents our experimental results, which show how the thermocapillary Marangoni effect influences the front mobility as well as the evolution of the drop thickness close to the contact line. Our experimental setup allows us to explore in detail this thickness, and its experimental and theoretical analysis is one of the main focal points of the present work. Next, we develop a theoretical model, based

on the lubrication approximation, and involving all relevant physical mechanisms. This approach yields a single governing equation for the evolution of the drop thickness, and allows for the specification of a desired temperature profile. We compare the model predictions and the experimental data for the part of the drop for which experimental data are available. Here, we concentrate on the qualitative comparison since the simulated drops are smaller than the experimental ones for computational reasons. Then, we discuss the model predictions in the regime where we do not have available experimental data. We will see that the final drop shape shows strong dependence on the imposed temperature profiles. In particular, one of the gradients considered here is predicted to lead to the occurrence of an interesting feature—a pronounced ridge in the transition region between the main body of the drop and the thin film close to the contact line. We conclude with a discussion regarding the connection between this drop profile and the Marangoni effect.

II. EXPERIMENTS

The experimental apparatus that we use is identical to the one discussed in detail in [30]; here, we only outline the key points. The basic apparatus consists of a prewetted silicon substrate placed on top of and in a good thermal contact with a cylindrical stainless steel base, see Fig. 1. The thickness of the substrate is 150 μm. It is disk-shaped, measuring 101.6 mm in diameter, and its surface is oxidized and highly polished. The complete apparatus rests on an optical table. The radial temperature gradient is accomplished by pumping cooled water from the recirculating cooler to the center of the substrate, while its periphery is heated via a metal foil heater attached to the outer copper ring, as indicated in Fig. 1. The temperature of the substrate is continuously monitored using radially embedded thermistors with an accuracy of ± 0.1 K. The main feature of the apparatus is that it allows for the generation of controlled radial temperature profiles that may be modified by tuning the heating or cooling sources and/or varying the initial drop size. The typical time scale on which the temperature of the substrate equilibrates is $\sim O(10^3)$ s. While

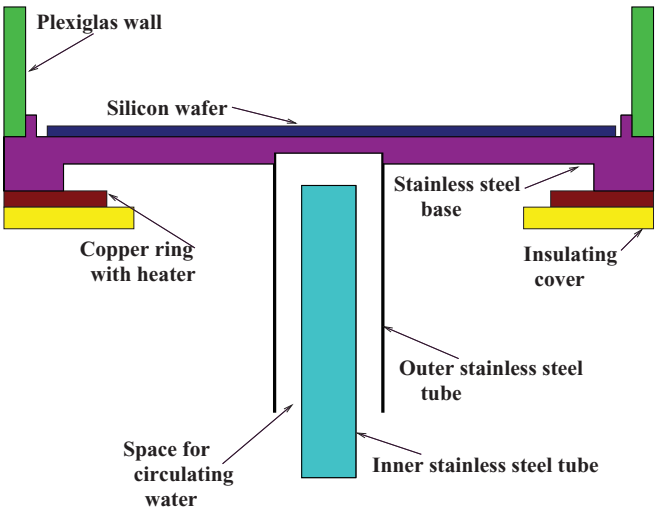

FIG. 1. (Color online) Sketch of the experimental apparatus.

various temperature profiles could be achieved, monotonically increasing temperature in the outward radial direction is a common feature of all profiles due to the positioning of the cooling pipe and heater in our experimental apparatus. Due to the competing effects of heating and cooling, however, the temperature in the center may be lower or higher compared to room temperature. We carry out experiments using drops of perfectly wetting nonvolatile 100cSt polydimethylsiloxane (PDMS). Due to the small vapor pressure of PDMS, evaporative cooling at the free surface is not relevant. Furthermore, the heat transfer at the gas-liquid interface turns out to be small, as can be verified by estimating the Biot number (see also [9,11]). In particular, $\mathrm{Bi} = \alpha_{\mathrm{th}} d_0/k \sim O(10^{-2}) \ll 1$, where $\alpha_{\mathrm{th}} \sim O(10)\mathrm{W}/(\mathrm{m}^2\ \mathrm{K})$ [10] is the interfacial heat transfer coefficient, $d_0 \sim O(10^{-4})$ m is the typical drop thickness at the center, and $k \sim O(10^{-1})\mathrm{W}/(\mathrm{mK})$ is the liquid thermal conductivity. Hence, the temperature of the free surface is for all practical purposes very close to the one prescribed by the heating apparatus in the substrate. The drops of prescribed volume are placed precisely at the center of the substrate. This is achieved using a specially machined device that guides the deposition from a micropipette. The radial precision of the deposition device is $\approx$0.1 mm. Particular drop sizes that we focus on are 50, 110, 150, 190, 400, and 750 mm^3. The drop and the substrate are partially shielded from the ambient air by an acrylic sidewall, and the drop remains axisymmetric throughout its evolution. The experiments are repeated to ensure reproducibility, and the substrate is thoroughly cleaned between experimental runs.

The imaging is carried out by illuminating the surface of the deposited drop from above using nearly monochromatic sodium vapor light with average wavelength $\lambda = 589$ nm. One portion of the light beam is reflected by the drop's free surface, the other by the highly polished substrate surface wetted by the drop. This generates an interference pattern where each fringe corresponds to a contour of a particular liquid thickness. The liquid thickness profile is reconstructed from the interference pattern by counting the fringes and recording their radial position. The counting is initiated from the nonwetted substrate slightly beyond the contact line position (where liquid thickness is taken to be zero), proceeding radially inward; each additional fringe corresponds to a $\lambda/(2n)$ increase in liquid thickness, where $n = 1.4$ is the refractive index for PDMS; the measurement of the radial position of each fringe relies on pixel-counting. Therefore, the accuracy of this technique is prescribed solely by the pixel size: the error in radial measurements is ± 50 μm. We note that temperature measurements do not rely on pixel counting and hence do not suffer from this source of error. For the liquid-solid combination we use here, the described technique allows for capturing liquid thickness in the range $[0.21, 10]$ μm. This interferometric technique does not work for thicker layers, because it is no longer possible to distinguish fringes.

The experiments proceed as follows. A PDMS drop is deposited at the center of the substrate, initially at the ambient temperature ($T = T_{\mathrm{room}} = 25\,^{\circ}$C.) The temperature-controlling apparatus is switched on as the spreading drop achieves 10 mm in diameter. The target temperature profile is cold at the center of the solid and hot at the periphery (since the

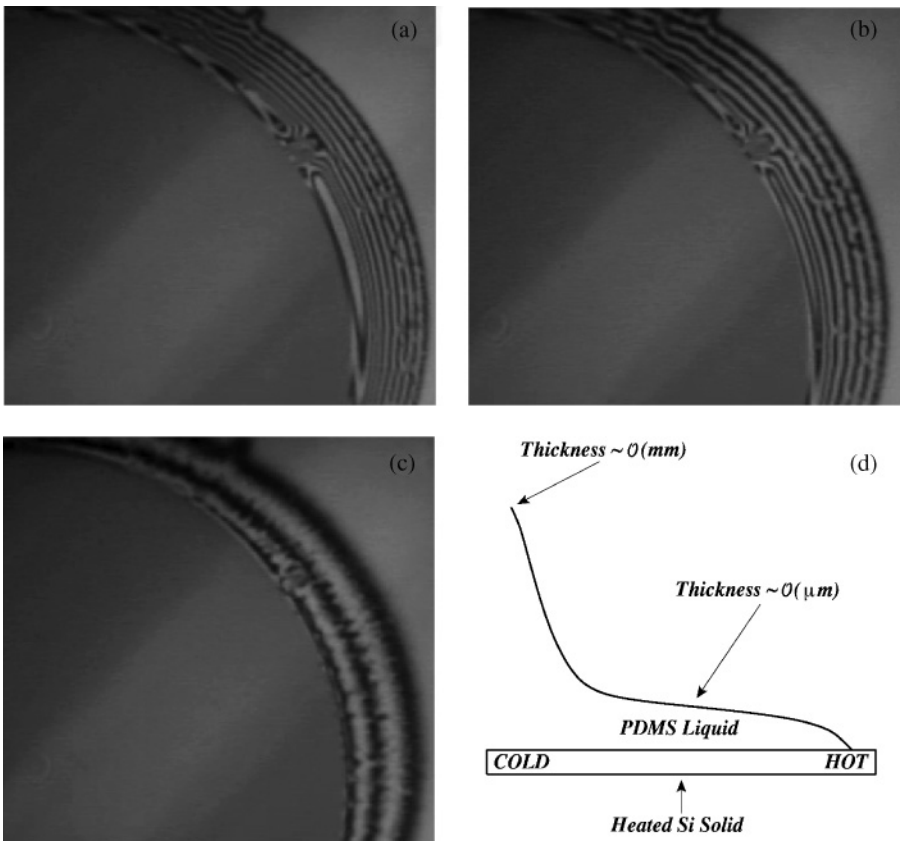

FIG. 2. Evolution of the contact line region for a 150 mm^3 PDMS drop on a heated Si substrate: (a) 10 000 s, (b) 15 000 s, and (c) 54 000 s after equilibration of the substrate temperature [the corresponding temperature profile is shown in Fig. 4(b)]. The field of view is 25 × 25 mm; maximum drop radius is 19.3 mm. The schematic in (d) illustrates the typical cross section of the region close to the contact line.

temperature in the center is set by the recirculating cooler, it is in general not equal to T_{room}). As the drop spreads, the slowly increasing temperature gradient at the drop's free surface induces thermocapillary Marangoni stresses directed from the contact line toward the center of the drop. However, since PDMS is completely wetting, the drop spreading continues despite the imposed (and slowly equilibrating) temperature gradient for another $\sim O(10^3)$ s; during this time, the gradient causes ever increasing deviation from Tanner's law [31]. Eventually, the oppositely directed Marangoni and capillary forces balance, halting the spreading, as the temperature profile finally reaches equilibrium. In the discussion below, we ignore the first ≈1000 s, the period that is marked by a time-dependent temperature profile and drop spreading. We focus solely on the details of the subsequent evolution involving slowly receding motion due to the influence of the steady-state temperature profile. The receding motion occurs on a much longer time scale, $\sim O(10^5)$ s, than the initial spreading stage, and the contact line moves very slowly, ∼0.1 mm/h. A typical evolution that we observe during the receding stage is shown in Fig. 2, which results from the temperature profile shown below in Fig. 4(b). We note that the liquid thermal diffusivity is $\kappa \sim O(10^{-7})$ m^2/s; using a length scale of the typical drop radius $L \sim O(10^{-2})$ m, and a velocity scale as prescribed by the receding motion of the contact line, $U \sim O(10^{-8})$ m/s, the resulting thermal Peclet number is small: $\text{Pe}_{\text{th}} = UL/\kappa \sim O(10^{-3}) \ll 1$. Even during spreading stage, where the initial $U \sim O(10^{-6})$ m/s, $\text{Pe}_{\text{th}} \sim O(10^{-1})$. Therefore, convection of heat in the liquid may safely be neglected [21].

An interesting feature is observed at the onset of the receding stage. Namely, the bulk of the drop tends to migrate toward the center of the solid substrate, due to the radially inward Marangoni stress along the free surface. This occurs at a rate that far exceeds the slow receding motion of the contact line itself, causing "stretching" of the thin layer of the liquid in the immediate vicinity of the contact line; see the sketch in Fig. 2(d). The slow motion of the contact line is likely caused by the wetting nature of PDMS, which effectively resists the inward Marangoni force. The dynamics we observe here is different from that in the receding meniscus problem, occurring when a solid plate is withdrawn from a bath [32], since there, in contrast, a partially wetting liquid is used and the effect of gravity is more important. The typical thickness near the center of the drop is estimated to be $\sim O(10^{-4})$ m, while the typical thickness of the thin layer close to the contact line, h_{max}, is several orders of magnitude smaller. This thin layer of liquid leads to the rings of interference fringes in Figs. 2(a)–2(c). Hence, we are able to monitor the evolution of its thickness. As the evolution proceeds, the density of interference fringes decreases [see, i.e., Fig. 2(b) compared to 2(c)], indicating that the thickness of the thin liquid layer decreases with time. This is confirmed by Fig. 3, which shows the time evolution of the thin layer thickness for a 150 mm^3 drop. This thin layer connects at its inner edge with the main body of the drop. This connection occurs over a relatively short region with a strong change in slope; over a radial distance of only a few millimeters, the liquid thickness changes from $O(\mu\text{m})$ to almost $O(\text{mm})$. Figure 3 also indicates that the rate of thinning decreases as the experiment proceeds. Since with

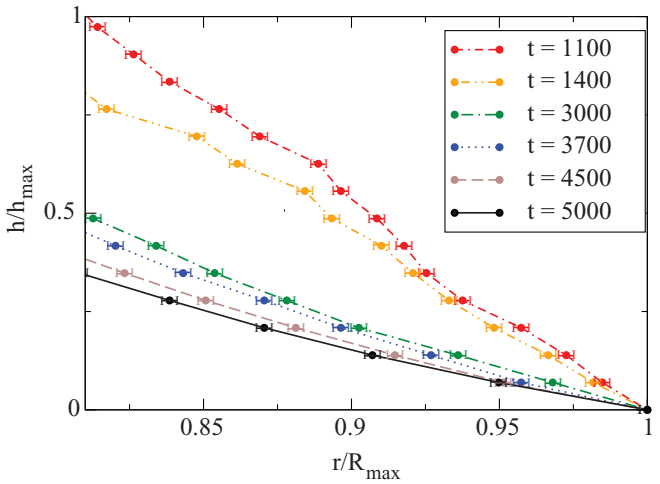

FIG. 3. (Color online) Experimental data: thickness evolution of the contact line region for a 150 mm^3 PDMS drop; $R_{max} = 19.3$ mm, $h_{max} = 3.3$ μm, and $t_{scale} = 3.7$ s. The imposed temperature gradient is given in Fig. 4(b). Error bars characterize experimental error in radial measurements. The thinning is monotonous in time.

the interference technique described above we can only probe the thin liquid layer close to the contact line, this transition region remains unresolved, but it will be discussed in the context of our theoretical model later in the paper. We also carry out experiments using different drop volumes, and find qualitatively similar dynamics (up to the level of experimental accuracy noted above) close to the contact line for all drop sizes: within the considered range of volumes, the drop size appears only to affect the time scale on which the described dynamics occurs. In what follows, we will present the results for two drop volumes, 150 and 750 mm^3, as representative examples.

Next, we examine the relation between the details of the imposed temperature profile and the thinning of the liquid layer close to the contact line. We introduce the following scales: the radial distance is scaled with $R_{max} \sim O(10^{-2})$ m, the drop radius at the onset of the receding motion (this instant in time is from here on denoted by $t = 0$); the thickness of the liquid is scaled with $h_{max} \sim O(10^{-6})$ m. Here, h_{max} is defined as the maximum measured thickness of the thin liquid layer inside the experimental window of observation, r/R_{max} in the interval $[0.81, 1]$. The time is scaled by ${R_{max}}^2/\nu$, where $\nu = 10^{-4}$ m^2/s is the kinematic viscosity of PDMS [$t_{scale} \sim O(s)$]. Finally, the difference between the temperature at any particular radial position and the temperature at the center of the drop, T_{center}, is scaled against T_{room} (all in °C). Typical values for T_{center}/T_{room} are within the range $[0.70, 1.42]$. We note that since the film thins, h_{max} always occurs in the first available measurement after $t = 0$. These scales are employed in Fig. 3 and all figures henceforth; they allow for direct comparison between the data for different drop sizes, as well as for subsequent comparison between the experiments and the predictions of the theoretical model derived in the following section.

Figure 4 shows the imposed temperature gradient and its influence on the evolution of the thin liquid film close to the contact line. The temperature profile in Fig. 4(b) leads to the results already shown in Figs. 2 and 3. It maintains most of the drop's free surface at a uniform temperature with a strong temperature gradient restricted to the contact line region. Figure 4(a) shows an alternative temperature profile characterized by an approximately linear increase of the temperature. Here, the temperature gradient in the contact line region is an order of magnitude smaller than the one corresponding to the profile in Fig. 4(b): 0.04 versus 0.4 °C/mm. The corresponding evolution of liquid layers for these two temperature profiles is shown in Figs. 4(c) and 4(d) [to facilitate the comparison, Fig. 4(d) shows the early time profiles already presented in Fig. 3]. We observe that for smaller temperature gradient, thinning is less pronounced. This finding supports our hypothesis regarding the connection between the Marangoni effect and the thinning of the liquid in

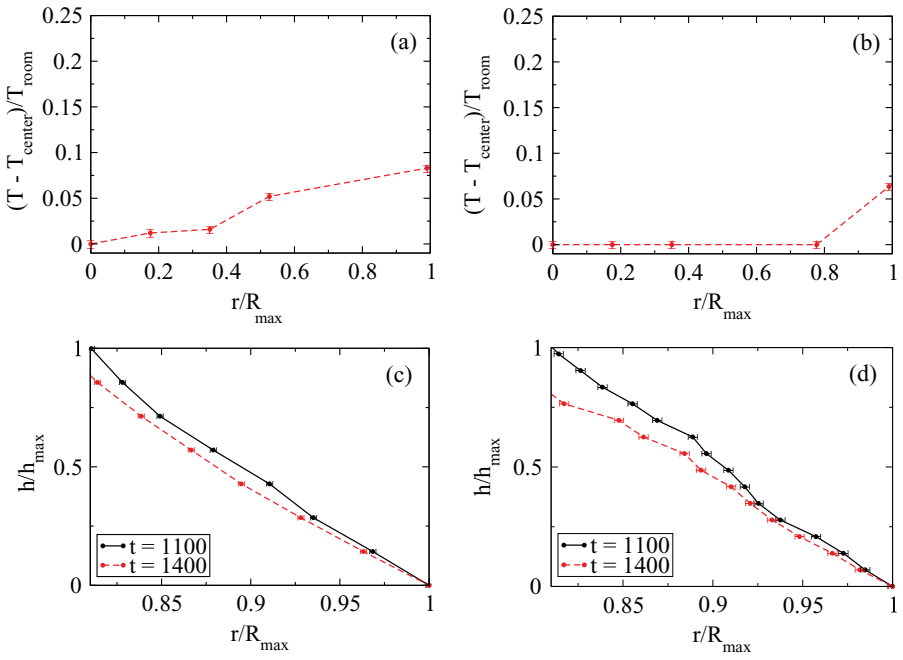

FIG. 4. (Color online) Experimental data for PDMS drops: influence of imposed temperature gradient on the evolution of the film thickness in the contact line region. The temperature profiles in (a) and (b) result in the thickness evolution in (c) and (d), respectively. Here, $(V, R_{max}, h_{max}, t_{scale}, T_{center}) =$ (750 mm^3, 28.5 mm, 2.2 μm, 8.1 s, 17.5 °C) in (a) and (c), and (150 mm^3, 19.3 mm, 3.3 μm, 3.7 s, 42.4 °C) in (b) and (d). Note that the scales R_{max}, h_{max}, and t_{scale} are different, as explained in the text. Error bars characterize experimental error in temperature, (a) and (b), and radial measurements, (c) and (d).

the contact line region, which we discuss in more detail in the following section.

III. THEORETICAL MODEL

We proceed by developing a theoretical model including all the relevant physical mechanisms. The predictions of the model will be compared to the experimental data presented in Fig. 4.

The foundations of the model are laid through the following assumptions: the aspect ratio of the drop is small, so that the lubrication approximation is appropriate; the solid substrate is heated nonuniformly, with a gradient in the radial direction, and this gradient is constant in time; the thermocapillary Marangoni effect is included via consideration of a temperature-dependent surface tension. While the formulation of this model is similar to the one used for studying drop evaporation [33,34], here evaporative mass loss is neglected due to the nonvolatility of PDMS for the present experimental conditions. Hence, evaporative cooling is also neglected, and the temperature profile at the liquid-gas interface is identical to the one in the substrate. In addition, we focus only on the dynamics subsequent to the temperature equilibration in the substrate, i.e., the initial transient behavior is ignored. Gravity is maintained in the formulation for completeness, although its influence is weak on the scales considered.

The basic setup that we consider involves an axisymmetric drop in simplified two-dimensional (2D) polar geometry. The origin of the reference frame is located at the center of the drop (situated on the solid surface), the r axis is measured radially from the center, and the z axis normal to the solid. Our model is based on the Navier-Stokes equations for a viscous incompressible liquid, accompanied by the continuity equation, and the appropriate boundary conditions: specification of temperature, and no slip and no penetration at the liquid-solid interface, $z = 0$; and the kinematic condition, as well as the balance of normal and shear stress at the liquid-gas interface $z = h(r,t)$, where h denotes the liquid thickness, evolving in time, t. The time when the temperature in the solid achieves equilibrium is denoted by $t = 0$. The temperature of the liquid, $T = T(r)$, is prescribed by the substrate heater, and it is kept explicitly in this formulation to allow for an easy switch between various temperature profiles.

The following scales are used to nondimensionalize the equations and boundary conditions. We use these scales (different from those used in the previous section) for the purpose of formulating the model in the form resembling those typically found in the literature (see, e.g., [35]); for convenience, all the results will be expressed in the scales used to describe the experimental results. The length scale is given by d_0, the typical drop thickness at the center ($r = 0$); the time scale is ${d_0}^2/\nu$; the velocity scale is ν/d_0; the scale for the liquid pressure is given by $(\rho\nu^2)/{d_0}^2$, where ρ is liquid density; finally, the difference between the liquid temperature, T, and the room temperature, T_{room}, is scaled by $\Delta T = T_{\max} - T_{\text{room}}$, where $T_{\max}$ is the maximum temperature achieved by the heater (a slightly different temperature scale is used below when comparing the model predictions and the experiments). Appropriate values of parameters that we use below are $d_0 = 7.5 \times 10^{-5}$ m, $\nu = 10^{-4}$ m^2/s, $\rho = 966$ kg/m^3, $T_{\text{room}} = 298$ K, and $T_{\max} = 335$ K. After scaling and applying the lubrication approximation in a manner similar to [35], the following nondimensional governing equation for the evolution of thickness $\bar{h}(\bar{r},\bar{t})$ of a radial drop results [34] (in the present work, all nondimensional quantities are barred):

$$\bar{h}_{\bar{t}} + \frac{1}{\bar{r}} S\left[\bar{r}\bar{h}^3\left(h_{\bar{r}\bar{r}\bar{r}} + \frac{1}{\bar{r}}\bar{h}_{\bar{r}\bar{r}} - \frac{1}{\bar{r}^2}\bar{h}_{\bar{r}}\right)\right]_{\bar{r}} - \frac{1}{\bar{r}} G[\bar{r}\bar{h}^3\bar{h}_{\bar{r}}]_{\bar{r}} - \frac{1}{\bar{r}}\mathcal{M}[\bar{r}\bar{h}^2\bar{T}_{\bar{r}}]_{\bar{r}} = 0, \tag{1}$$

where subscripts denote derivatives. Here, the last three terms are due to surface tension, gravity, and the Marangoni effect, respectively. The Marangoni term involves the liquid temperature, $\bar{T}(\bar{r})$, which is to be prescribed (see below). We note that in the formulation given by Eq. (1), both $\bar{h}$ and $\bar{r}$ are expressed in terms of d_0. Therefore, the validity of the lubrication approximation requires that all nondimensional slopes are small. The nondimensional coefficients are defined as follows:

$$S = \frac{\sigma_0 d_0}{3\rho\nu^2}, \quad G = \frac{d_0^3 g}{3\nu^2}, \quad \mathcal{M} = \frac{\gamma\Delta T d_0}{2\rho\nu^2},$$

corresponding to nondimensional surface tension, gravity coefficient, and modified Marangoni number, respectively. A linear dependence of surface tension on the temperature is assumed: $\sigma(T) = \sigma_0 - \gamma(T - T_{\text{room}})$, where $\sigma(T_{\text{room}}) = \sigma_0 = 2.1 \times 10^{-2}$ N/m and $\gamma = -d\sigma/dT = 5.2 \times 10^{-5}$ N/(m K), see, e.g., [36]; g is the gravitational acceleration. Resulting values of nondimensional coefficients are $S = 5.4 \times 10^{-2}$, $G = 1.4 \times 10^{-4}$, and $\mathcal{M} = 7.5 \times 10^{-3}$.

The temperature profiles, $\bar{T}(\bar{r})$, are based on the experimental ones. One profile (A) that we consider is a linear function of $\bar{r}$, and it mimics the linear profile from the experiments, Fig. 4(a): $\bar{T}(\bar{r}) = \bar{T}(0) + m\bar{r}$, where $\bar{T}(0)$ and slope m are prescribed below, is substituted into Eq. (1). For the temperature profile B, we require that most of the drop lies in a region where the temperature field is essentially constant (within the experimental accuracy), with substantial temperature gradient occurring only in the contact line region, as in the experimental profile in Fig. 4(b). Here, we recall that in the steady-state case, $\bar{T}(\bar{r})$ satisfies Laplace's equation on a disk with a fixed temperature at the perimeter—a particular solution to this Dirichlet problem is $\bar{T}(\bar{r}) = C_1 \ln\bar{r} + C_2$ for $\bar{r} > 0$ (C_1, C_2 are constants). Furthermore, we require that the temperature is C^2 continuous throughout the domain to avoid any possible numerical issues, and that it reaches a prescribed value at $\bar{r} = 0$. One appropriate form is given by

$$\bar{T}(\bar{r}) = \begin{cases} \alpha + \exp(\ln\beta + \delta\ln\bar{r}), & \bar{r} < R_c/d_0, \\ \theta + \chi\ln\bar{r}, & \bar{r} \geqslant R_c/d_0, \end{cases} \tag{2}$$

with the five coefficients $(\alpha,\beta,\delta,\theta,\chi)$ determined by the five conditions specified above; their values are listed in the next section. Here, R_c denotes the radial distance where the transition between essentially constant temperature for $r < R_c/d_0$ and strong temperature gradients takes place. Next, we carry out numerical simulations of Eq. (1) using the temperature profiles A and B, and compare the results with the experimental data.

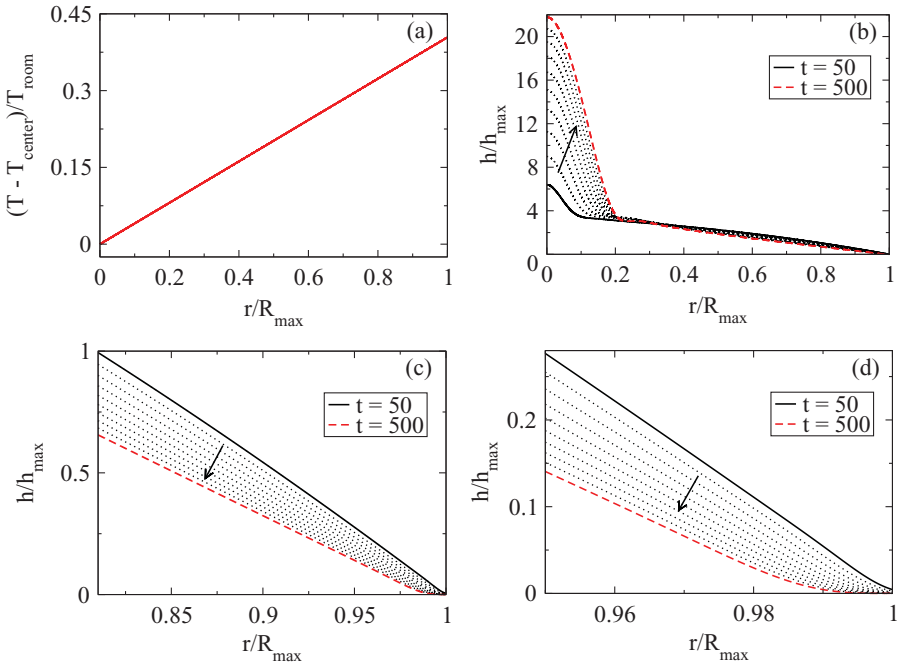

FIG. 5. (Color online) (a) Temperature profile A. Evolution of the drop thickness: (b) whole drop, (c) thin-film region, and (d) contact line detail. Here, $h_{\max} = 4.2$ μm; the other scales are given in the text for this and all consecutive figures. Thickness profiles in (b), (c), and (d) are given at every 50 time units.

IV. NUMERICAL RESULTS VERSUS EXPERIMENTAL DATA

The main goal of our simulations is to show qualitative agreement of the results with the experimental data in the regime where experimental data are available (close to the contact line), and to obtain clear predictions in the regime where experimental data are not available. To this end, Eq. (1) is solved numerically using a finite-difference-based code, similar to the one used in [34]. Here, we only outline the main points of our approach; the details are given in [37]. Equation (1) is a parabolic fourth-order one. As a result, it is a stiff partial differential equation (PDE), suggesting the use of implicit schemes due to stability concerns. We employ a Crank-Nicholson scheme for time discretization, with adaptive time-stepping. For space discretization, a compact stencil central-difference scheme is used with the grid size $\Delta r = 0.006$ in all simulations. This numerical approach is second-order convergent in both time and space. The boundary conditions ensure conservation of mass. The nonlinearity of Eq. (1) is treated using Newton's method, leading finally to a a pentadiagonal linear system to be solved within each Newton iteration. The difficulty of simulating contact line motion is overcome via the addition of a thin equilibrium layer of thickness d_p, which is assumed to wet the numerical domain with the drop positioned on top of it. See, e.g., Appendix A of [38] for a rather detailed description of this approach and its relation to the disjoining pressure model. In the present work, due to complete wetting of PDMS on Si, this approach effectively leads to the presence of equilibrium film, as mentioned above. In our simulations, to ensure convergence, we use $\Delta r < d_p$ in all simulations. The smallness of Δr requires, however, a large number of grid points. This large number can be reduced by using nonuniform computational grids, but we do not attempt this in the present work. Therefore, to carry out well-resolved and accurate simulations while using reasonable computational resources, we limit our simulations to 5 mm^3 drops, smaller than in experiments. While these smaller volumes prevent us from carrying out a quantitative comparison between numerical and experimental results, we expect that the main features of the results will be captured. For a drop size of 5 mm^3, it is appropriate to use $d_0 = 7.5 \times 10^{-5}$ m. All simulations use $d_p = 5 \times 10^{-7}$ m, since for the d_p's of this order, we do not see any influence of their precise value on the resulting drop evolution. The smooth initial condition is developed from a spherical cap profile, evolved using a version of our code with $T = T_{\text{room}}$ (i.e., spreading over a nonheated solid) until the drop radius reaches a value corresponding to the experimentally measured $R_{\max}$. All simulations preserve initial fluid mass.

We carry out simulations using the temperature profiles A (linear) and B [given by Eq. (2)]. To allow for the comparison between the computational results of the models A and B, and also with the experimental data, we choose temperature-related parameters such that the temperature difference $T(R_{\max}) - T(0)$ resulting from the two temperature profiles is identical. Figures 5(a) and 6(a) show the profiles A and B, respectively. For profile A, $\bar{T}(0) = 0.1105$ and $m = 1.517 \times 10^{-3}$; for profile B, $\alpha = \bar{T}(0)$, $\ln\beta = -169.1$, $\delta = 32.54$, $\theta = -2.103$, and $\chi = 0.4397$. The scales we use for presenting the results of numerical simulations are the ones defined in the experimental section. We use $R_{\max} = 15.7$ mm, $t_{\text{scale}} = 2.5$ s, and $T_{\text{center}} = 24.09\,^{\circ}$C for all the results given in this section. Note that $h_{\max}$ depends on the applied temperature profile. Its value is taken at the first output time, $t = 50$.

First, we concentrate on temperature profile A. Figure 5(c) shows the corresponding evolution of the film thickness in the region close to the contact line ($0.81 \leqslant r/R_{\max} \leqslant 1$, as in the experiments). While the contact line is mobile, this motion is very slow; Fig. 5(d) shows the values of the speed $\approx$0.5 mm/h, the same order of magnitude as in the experiments. The thinning shown in Figs. 5(c) and 5(d) is a

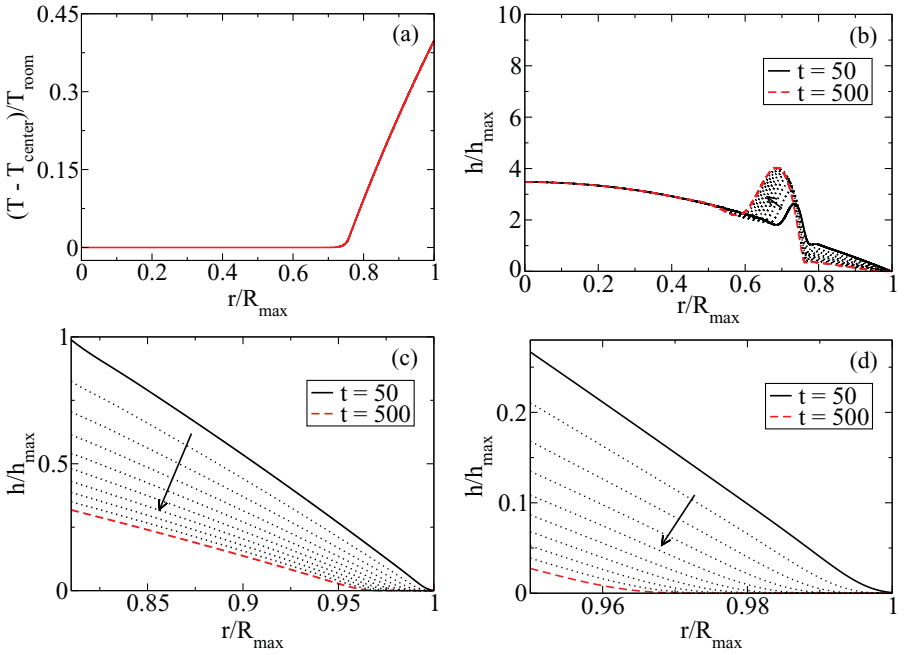

FIG. 6. (Color online) (a) Temperature profile B. Evolution of the drop thickness: (b) whole drop, (c) thin-film region, and (d) contact line detail. Here, $h_{max} = 3.7\ \mu$m. Thickness profiles in (b), (c), and (d) are given at every 50 time units.

consequence of the Marangoni force that is directed inward, from the contact line toward the center of the drop; this behavior is consistent with the experimental data from Fig. 4(c) resulting from the similar linear temperature profile shown in Fig. 4(a). The linear temperature profile induces inward Marangoni force everywhere along the drop surface, driving the liquid consistently toward the center of the drop. Liquid accumulates in the region close to $r = 0$, leading to a marked increase in film thickness there, as shown in Fig. 5(b). As pointed out before, experimental data are not yet available on the scale of the whole drop, and therefore at this point the profile as shown in Fig. 5(b) is a prediction of the expected outcome.

Figure 6 shows the results obtained using the temperature profile B. We note that the contact line recedes faster compared to Fig. 5. This is not surprising due to increased temperature gradient close to the contact line. Consistently, we find that the thinning of the liquid layer for profile B is more pronounced compared to the profile A, viz., Figs. 6(c) and 5(c). Our theoretical model is therefore successful in capturing qualitatively the behavior observed in the experiments and shown in Fig. 4. The thinning shown in Figs. 6(c) and 6(d) is also in agreement with the experimental data in Figs. 2 and 3 for similar temperature gradients. In particular, it indicates that the rate of thinning decreases in time, qualitatively matching the experimental results in Fig. 3.

Figure 6(b) shows the thickness evolution of the whole drop and reveals the formation of a ridge slightly inward from the region monitored in Fig. 6(c). The peak of this ridge moves slowly inward, although this motion slows down as the evolution progresses. Figure 7 suggests that the ridge reaches a steady position, corresponding closely to the transition point in the temperature gradient, R_c, and confirming that ridge formation is a consequence of Marangoni forces. Additional simulations (not shown here for brevity) support this conclusion.

The experimental images in Figs. 2(a)–2(c) support the possibility of ridge formation. They show an accumulation of interference fringes close to the transition between the thin liquid layer in the contact line region and the main body of the drop. Hence, a substantial increase in liquid thickness may be occurring in this transition region. The effective range of our experimental technique does not allow for precise measurements there. We leave it to future experiments to verify directly this prediction of our theoretical model for the thickness characteristic of this region.

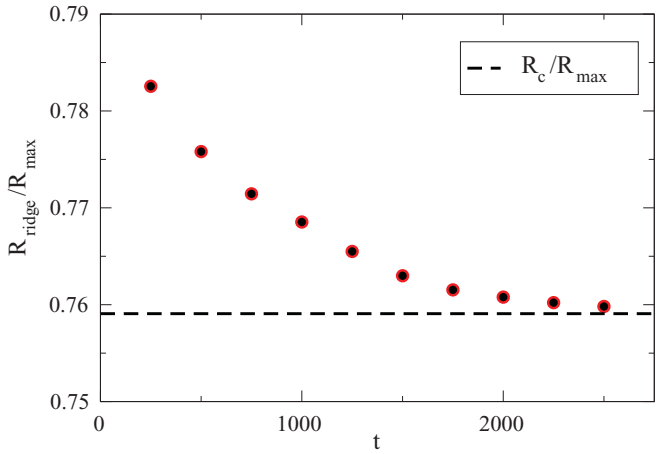

FIG. 7. (Color online) Long-time evolution resulting from temperature profile B, Fig. 6(a): the position of the maximum thickness of the ridge, R_{ridge}, compared to R_c, the transition point in the temperature gradient.

V. CONCLUSIONS

Thermally driven free-surface flows of liquid have many applications of practical significance. We have studied flows involving drops of nonvolatile perfectly wetting liquid subjected to radial temperature gradients. In our experiments, we

witness the opposing action of the thermocapillary Marangoni effect and capillary spreading, and focus on the receding phase where the balance has already swung in favor of the former effect. We record an interesting feature that develops during this phase—while the bulk of the drop mass recedes toward the center, the contact line recedes at a much slower rate, leaving a stretched layer of liquid between the main body of the drop and the contact line. We find that this layer of liquid thins as evolution of the drop proceeds and that the thinning is more pronounced when the imposed temperature gradient in the contact line region is larger. This trend is reproduced by our theoretical model, based on the long-wave approximation, which includes Marangoni forces. Our model also indicates a strong dependence of the drop shape on the imposed temperature gradient, and, for a particular class of temperature profiles, it predicts the formation of a ridge between the thin liquid layer and the main body of the drop. We expect that this prediction will be verified by future experiments.

ACKNOWLEDGMENTS

S.M. would like to thank Richard McLaughlin for extensive discussions, and Richard Nappi for his help in the machine shop. This work was partially supported by NSF Grants No. DMS-0244498 (S.M., R.P.B.), No. DMS-0968252 (R.P.B.), and No. DMS-0908158 (L.K.).

[1] D. E. Kataoka and S. M. Troian, Nature (London) **402**, 794 (1999).
[2] G. L. Liu, J. Kim, Y. Lu, and L. P. Lee, Nat. Mater. **5**, 27 (2006).
[3] R. H. Farahi, A. Passian, T. L. Ferrell, and T. Thundat, Appl. Phys. Lett. **85**, 4237 (2004).
[4] C. Huh and L. E. Scriven, J. Colloid Interface Sci. **35**, 85 (1971).
[5] A. L. Bertozzi, Notices Am. Math. Soc. **45**, 689 (1998).
[6] D. Bonn, J. Eggers, J. Indekeu, J. Meunier, and E. Rolley, Rev. Mod. Phys. **81**, 739 (2009).
[7] P. Ehrhard and S. H. Davis, J. Fluid. Mech. **229**, 365 (1991).
[8] M. K. Smith, J. Fluid. Mech. **294**, 209 (1995).
[9] D. E. Kataoka and S. M. Troian, J. Colloid Interface Sci. **192**, 350 (1997).
[10] D. E. Kataoka and S. M. Troian, J. Colloid Interface Sci. **203**, 335 (1998).
[11] J. M. Davis, D. E. Kataoka, and S. M. Troian, Phys. Fluids **18**, 092101 (2006).
[12] S. W. Benintendi and M. K. Smith, Phys. Fluids **11**, 982 (1999).
[13] M. A. Clay and M. J. Miksis, Phys. Fluids **16**, 3070 (2004).
[14] A. Oron and P. Rosenau, J. Phys. II (France) **2**, 131 (1992).
[15] A. Oron and P. Rosenau, J. Fluid. Mech. **273**, 361 (1994).
[16] U. Thiele and E. Knobloch, Physica D **190**, 213 (2004).
[17] A. Moosavi, M. Rauscher, and S. Dietrich, J. Chem. Phys. **129**, 044706 (2008).
[18] A. Oron, S. H. Davis, and S. G. Bankoff, Rev. Mod. Phys. **69**, 931 (1997).
[19] R. V. Craster and O. K. Matar, Rev. Mod. Phys. **81**, 1131 (2009).
[20] A. M. Davis, F. Heslot, S. M. Troian, and P. Carles, Nature (London) **346**, 824 (1990).
[21] K. D. Barton and R. Shankar Subramanian, J. Colloid Interface Sci. **133**, 211 (1989).
[22] J. Sur, A. L. Bertozzi, and R. P. Behringer, Phys. Rev. Lett. **90**, 126105 (2003).
[23] S. Daniel, M. K. Chaudhury, and J. C. Chen, Science **291**, 633 (2001).
[24] A. D. Nikolov, D. T. Wasan, A. Chengara, K. Koczo, G. A. Policello, and I. Kolossvary, Adv. Colloid Interface Sci. **96**, 325 (2002).
[25] O. A. Kabov, Thermophys. Aeromech. **5**, 547 (1998).
[26] O. A. Kabov, B. Scheid, I. A. Sharina, and J. C. Legros, Int. J. Therm. Sci. **41**, 664 (2002).
[27] J. M. Skotheim, U. Thiele, and B. Sheid, J. Fluid. Mech. **475**, 1 (2003).
[28] S. Kalliadasis, A. Kiyashko, and E. A. Demekhin, J. Fluid. Mech. **475**, 377 (2003).
[29] C. Song, K. Kim, K. Lee, and H. K. Pak, Appl. Phys. Lett. **93**, 084102 (2008).
[30] S. Mukhopadhyay and R. P. Behringer, J. Phys.: Condens. Matter **21**, 464123 (2009).
[31] L. H. Tanner, J. Phys. D **12**, 1473 (1979).
[32] J. H. Snoeijer, G. Delon, M. Fermigier, and B. Andreotti, Phys. Rev. Lett. **96**, 174504 (2006).
[33] Y. Gotkis, I. Ivanov, N. Murisic, and L. Kondic, Phys. Rev. Lett. **97**, 186101 (2006).
[34] N. Murisic and L. Kondic, Phys. Rev. E **78**, 065301(R) (2008).
[35] J. P. Burelbach, S. G. Bankoff, and S. H. Davis, J. Fluid Mech. **195**, 463 (1988).
[36] *Handbook of Chemistry and Physics*, 78th ed., edited by D. R. Lide (CRC, New York, 1997).
[37] J. Diez and L. Kondic, J. Comput. Phys. **183**, 274 (2002).
[38] J. Diez and L. Kondic, Phys. Fluids **19**, 072107 (2007).